Chapter IV

Structural, Magnetic and Photocatalytic Properties of Mn Doped TiO_2 Nanoparticles

4.1 Introduction

In this chapter, we have discussed the structural modifications in TiO_2 nanoparticles after doping 1, 2 and 3 at% of Mn followed by calcination at 500 ºC. Structure and microstructure of these nanoparticles are elaborated in section 4.2 using XRD, Raman, TEM, BET and XPS. Magnetic properties are discussed in section 4.3. Section 4.4 describes the photocatalytic properties. In Section 4.5 antibacterial properties of the samples discussed followed by conclusions of this chapter in section 4.6.

4.2 Structure and Microstructure of Mn Doped TiO_2 Nanoparticles

4.2.1 X-Ray Diffraction and Raman Spectroscopy

$Ti_{1-x}Mn_xO_2$, where x= 0.01, 0.02 and 0.03 are named as TMn1, TMn2 and TMn3, respectively. X-ray powder diffraction patterns with Le-Bail profile fitting using FULLPROF program with pseudo-Voigt function are shown in Figure 4.1. The simulated XRD patterns of TMn1, TMn2 and TMn3, are fitted with anatase and rutile phase with space group $I4_1$/amd and $P4_2$/mnm, respectively. After fitting, the simulated data, observed patterns and the difference of observed to simulated data are shown as continuous black line, red dots and blue line, respectively. The green lines in between the fitted data and the difference patterns show the position of the Bragg peaks. The cell parameters and cell volume obtained from the refinements are tabulated in Table 4.1. The XRD patterns reveal well resolved and sharp diffraction peaks signifying the crystalline nature of the particles. No other peak corresponding to manganese oxide confirms that Mn ions substitute Ti site irrespective of anatase or rutile phase of TiO_2. TMn1 show (101), (103), (004), (112), (200), (105), (211), (204), (116), (220), and (215) peaks indexed as the anatase phase of TiO_2 with space group, $I4_1/amd$. Along with anatase phase, diffraction peaks, (110) at 27.5° and (101) at 36.3° associated to rutile phase of TiO_2, space group, $P4_2/mnm$ are also observed. Although both anatase and rutile phase are present in TMn2, the intensity of (110) corresponding to rutile phase decreases and disappears when Mn concentration reaches 3 at%. It is evident from the XRD pattern of TMn3 that observed diffraction peaks such as (101), (103), (004), (112), (200), (105), (211), (204), (116), (220), and (215) are matched well with anatase phase of TiO_2. No peak corresponding to rutile phase is observed. It is noteworthy to mention that irrespective of anatase/rutile phase, the lattice volume is significantly low compared to the bulk in all samples. Since the ionic radius of Mn ion is

Table 4.1 *Standard JCPDS data of TiO_2, anatase and rutile phase with refined experimental data of $Ti_{1-x}Mn_xO_2$ (x = 0.01, 0.02 and 0.03).*

Samples	a (Å)= b (Å)		c (Å)		Unit Cell Volume (Å^3)	
	Anatase	Rutile	Anatase	Rutile	Anatase	Rutile
TMn1	3.7821±0.0003	4.5881±0.0013	9.4996±0.0016	2.9588±0.0004	135.89	62.28
TMn2	3.7823±0.0001	4.5763±0.0004	9.5002±0.0006	2.9578±0.0003	135.91	61.95
TMn3	3.7830±0.0003	-	9.4895±0.0015	-	135.81	-
Standard Data	3.785	4.593	9.514	2.958	136.30	62.38

less than Ti ion, the Mn substitution at Ti site thus reduces the cell volume notably. Further, we have estimated the fraction of rutile phase from the XRD peak intensities with the help of following equation: $X_R = 1/[1 + 0.884(I_A/I_R)]$. X_R is the phase fraction of rutile phase, I_R and I_A are the X-ray-integrated intensities of (110) and (101) corresponding to rutile and anatase phase of TiO_2, respectively [Tian et al. (2011) and Chauhan et al. (2012)]. We found 8% of rutile phase in TMn1 that decreases with increasing Mn concentration and becomes pure anatase phase in TMn3.

In order to confirm observed structural transformation in Mn-doped TiO_2, we carry out Raman measurements. TiO_2 shows six strong Raman-active modes, such as, one A_{1g}, two B_{1g}, and three E_g modes in anatase phase [Sharma et al. (2011)]. The E_g modes appear at 144, 197 and 639 cm^{-1}, B_{1g} at 399 cm^{-1}, A_{1g} mode superimposed with B_{1g} at 513−519 cm^{-1}. However, rutile TiO_2 exhibits four Raman-active modes such as B_{1g}, E_g, A_{1g} and B_{2g} at 143, 447, 612 and 826 cm^{-1}, respectively [Ricci et al. (2013)]. Raman spectra of TMn1, TMn2 and TMn3, in the region of 100 to 800 cm^{-1} are shown in Figure 4.2. We observe E_g mode with the highest intensity at 147 cm^{-1}, two weak modes at 199 and 635 cm^{-1}, B_{1g} mode at 397 cm^{-1} and A_{1g}+B_{1g} at 514 cm^{-1}. Except E_g mode, other Raman modes are closely matched with the characteristic of anatase phase reported in literature [Sharma et al. (2011)]. Absence of Raman mode corresponding to rutile phase indicates meager amount of rutile one present in TMn1 and TMn2. The most intense mode E_g, located at143 cm^{-1} is due to O–Ti–O bending vibrations for anatase phase [Raut et al. (2012)]. Shifting of the peak to 147 cm^{-1} observed in all samples is because of the distortion in Ti–O bond, after Mn incorporation in TiO_2 lattice. No noticeable impurity related peaks observed in the Raman spectra confirm the pure phase of TiO_2 and corroborates with the XRD results. It may be noted that although anatase to rutile phase transformation is generally reported in TiO_2 either by tuning the size of the particles [Lu et al. (2003), Zhang et al. (1998) and Bahadur et al. (2012)], or by doping with different concentration of dopants like N, Mn and Co [Bu et al. (2012), Barakat et al. (2005), Fu et al. (2014) and Tseng et al. (2014)], we demonstrate here an unusual phase transformation from a mixed phase of rutile and anatase to pure anatase one by incorporating Mn in TiO_2 lattice. In contrast to our results, while Deng et al. (2011), show stable anatase phase with increasing Mn concentration upto 12 at%, Lu et al. (2012), observe rutile phase with Mn doping. Chauhan et al. (2012), does not observe any phase transformation with increasing calcination temperature from 300 to 700 ºC in Mn doped TiO_2. Particle size dependent phase transformation from anatase to rutile has been studied with dopant such as Ni and Co etc [Tian et al. (2011), Bahadur et al. (2012), Bagwasi et al. (2013) and Tseng et al. (2014)]. It has been suggested that thermodynamic phase stability of anatase TiO_2 is more than rutile one below particle size of 14 nm [Lu et al. (2003), Zhang et al. (1998) and Bahadur et al. (2012)]. In addition, several other parameters like surface area and pH of precipitation, contribute in deciding the phase transformation in nanocrystalline TiO_2 [Hu et al. (2003)a]. Lower the surface area, lower is the coarsening rate that leads to decrease in phase transition temperature. Previously, pH dependent anatase to rutile phase transformation has been reported by our group [Rath et al. (2009)a].

4.2.2 Transmission Electron Microscopy

Here an unusual phase transformation from the mixed phase of anatase and rutile to anatase has been understood from the view point of particle size and oxygen vacancy. The crystallite size using Scherrer's formula [$D = 0.9\lambda/\beta \mathrm{Cos}\theta$] has been estimated to be 13 nm and 8 nm for TMn1 and TMn3, respectively. Figure 4.3 (a) and (b) show transmission elec-

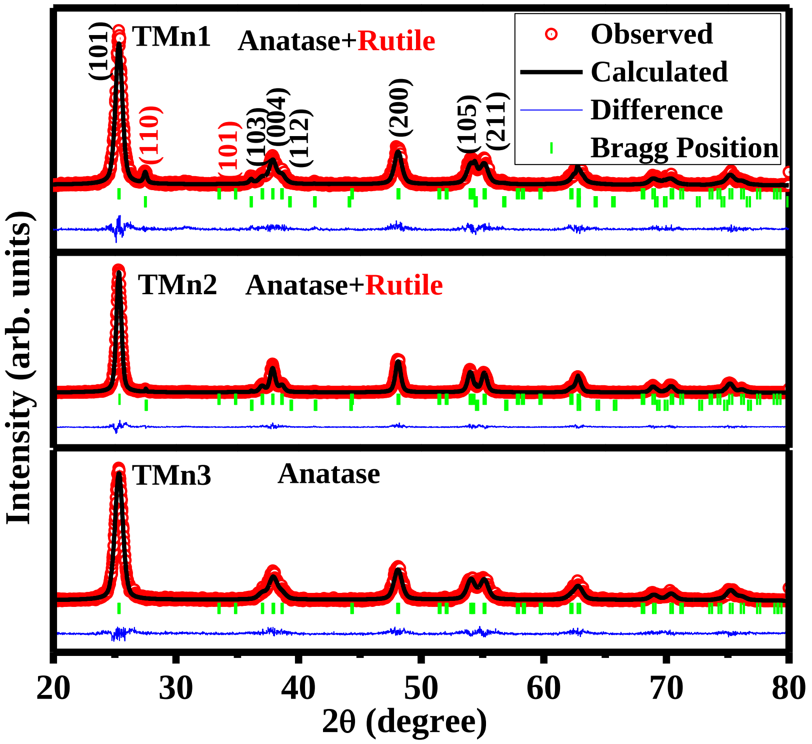

Figure 4.1 *Le-Bail profile fitting of XRD patterns of* $Ti_{1-x}Mn_xO_2$ *(x = 0.01, 0.02 and 0.03) using the FULLPROF program.*

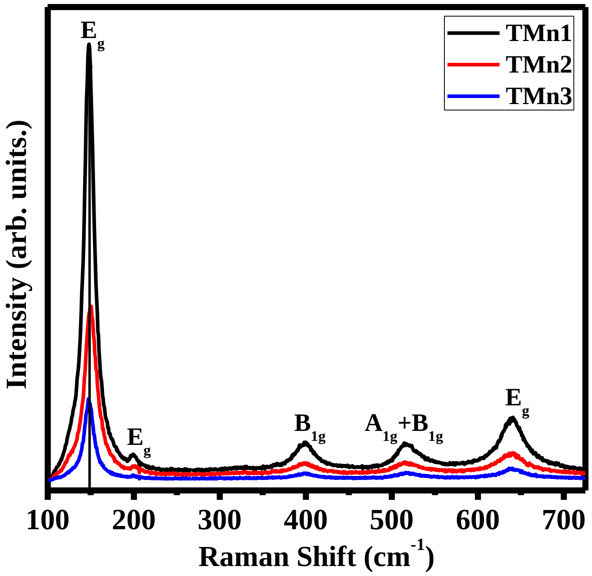

Figure 4.2 *Raman spectra of* $Ti_{1-x}Mn_xO_2$ *(x = 0.01, 0.02 and 0.03).*

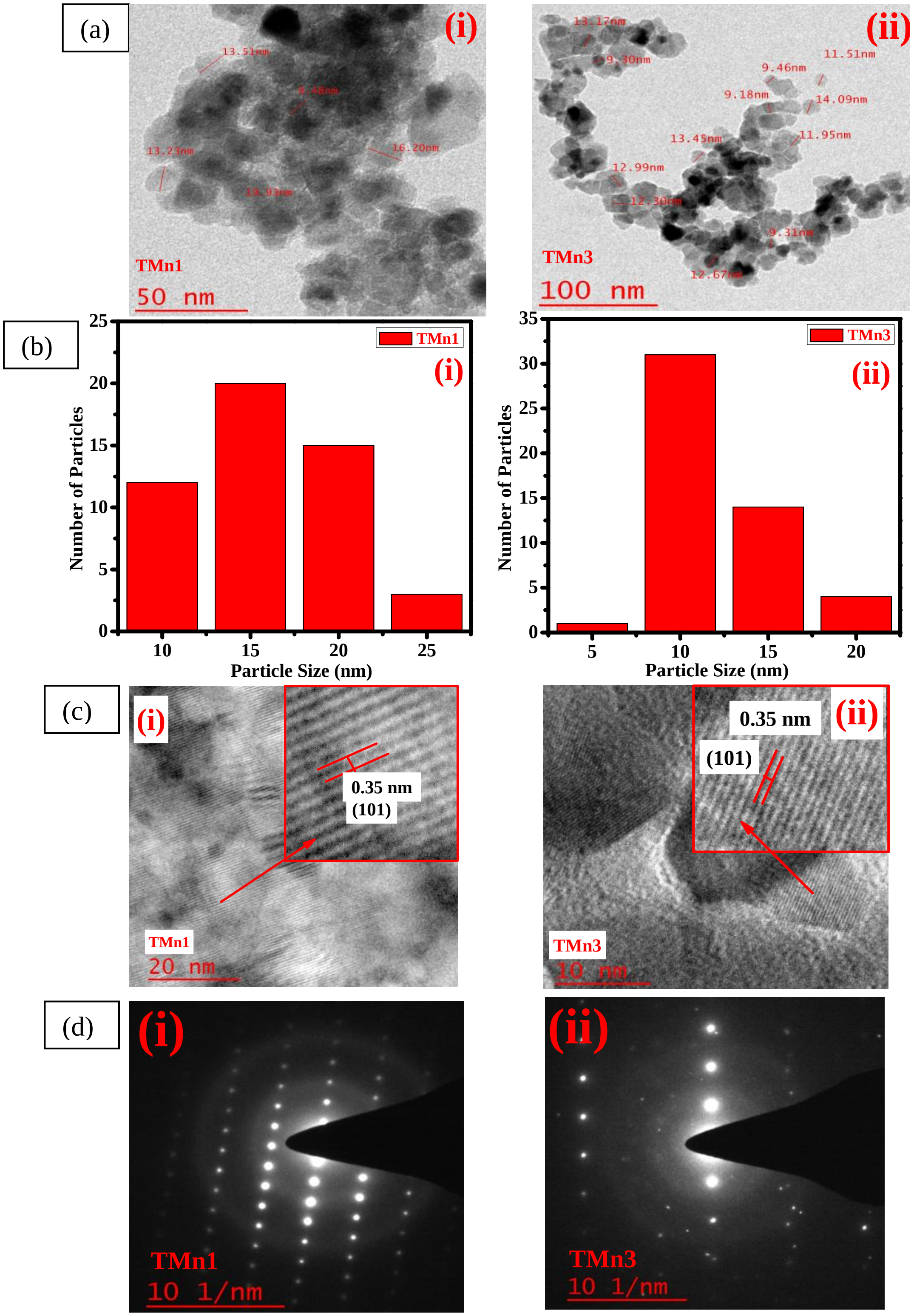

Figure 4.3 *(a) Bright field TEM images of* $Ti_{1-x}Mn_xO_2$ *(i) x= 0.01 and (ii) x= 0.03; (b) show particle size distribution, (c) HRTEM images and zoomed view of lattice planes, (d) SAED pattern.*

tron micrographs for TMn1, TMn3 and particle size distribution histogram, respectively. The average particle size for TMn1 and TMn3 is ~15 and 12 nm, respectively. The lattice fringes observed from HRTEM images (Figure 4.3 (c)) show inter-planar spacing of 0.35 nm, corresponding to (101) of anatase phase for both TMn1 and TMn3. The selected area electron diffraction (SAED) patterns shown in Figure 4.3 (d) indicate the single crystalline in nature of the particles. Comparing the particle size and crystallite size, it is confirmed that particles are single crystalline nature. One may notice that even with increasing Mn concentration, the particles remain below 15 nm which hinders the formation of rutile phase [Lu et al. (2003) and Zhang et al. (1998)]. Therefore, such an unusual phase transformation from anatase and rutile mixed phase to anatase phase has been observed in these single crystal particles with size less than 15 nm.

4.2.3 Porosity analysis through BET

Figure 4.4 (a) shows a typical pore structure using N_2 adsorption–desorption isotherm measurements. It shows adsorption isotherms of type IV for TMn1, which indicates typical

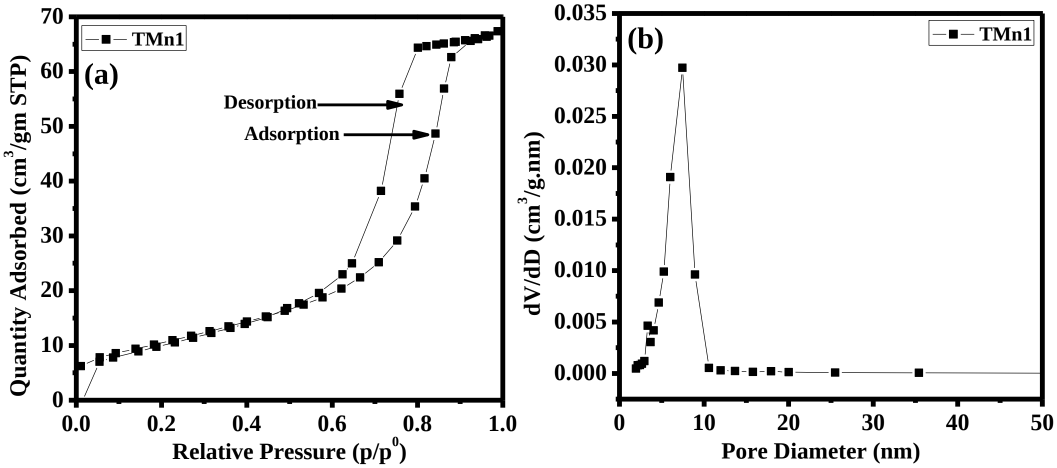

Figure 4.4 *(a) N_2 adsorption and desorption isotherms of TMn1, (b) shows pore size distribution curve.*

mesoporous nature of Mn doped TiO_2 with H1 type hysteresis loop, depicts that the sample is comprised of well defined cylindrical pores [Niu et al. (2013), Liu et al. (2016)]. The poresize distribution of TMn1, indicating that it has a narrow mesoporosity distribution with an average pore diameter about 6.67 nm shown in Figure 4.4 (b). The smaller average particle size and mesoporous nature of the Mn doped TiO_2 nanoparticles offer higher specific surface area for the photocatalytic reactions.

4.2.4 X-Ray Photoelectron Spectroscopy

The formation of oxygen vacancies is further determined from X-ray photoelectron spectroscopy (XPS). The asymmetric O 1s core level spectra shown in Fig. 4.5 (a) are fitted with two peaks named as Oa and Ob. Oa and Ob are attributed to the lattice oxygen (Ti‑O‑Ti) and hydroxyl groups respectively [Hu et al. (2003)a and Kim et al. (2012)]. The concentration of oxygen vacancies is quantified after taking the area ratio of peak Ob to Oa and the calculated values are found to be 0.02 and 0.19 for TMn1 and TMn3, respectively. The increase in area ratio value indicates the enhancement in concentration of oxygen vacancies with increasing Mn concentration, evoking the formation of anatase phase as reported by Choudhury et al. (2013)a. Due to the presence of oxygen vacancies, it is expected that Mn and Ti would have various oxidation states. In Figure 4.5 (b), XPS spectra of each Ti $2p_{3/2}$ and $Ti2p_{1/2}$ are fitted with two peaks, the peak at higher binding energy corresponds to Ti^{4+}, whereas, the peak at lower binding energy is attributed to Ti^{3+} state, owing to the presence of an oxygen vacancy next to a Ti atom [Kim et al. (2012) and Pham et al. (2014)]. It is observed that with increasing Mn concentration, Ti^{3+} ions increases. Figure 4.5 (c) depicts XPS spectra of Mn 2p indicating that the peaks are broad and asymmetric in nature, suggesting existence of Mn in different oxidation states [Deng et al. (2011)]. Mn $2p_{3/2}$ peak

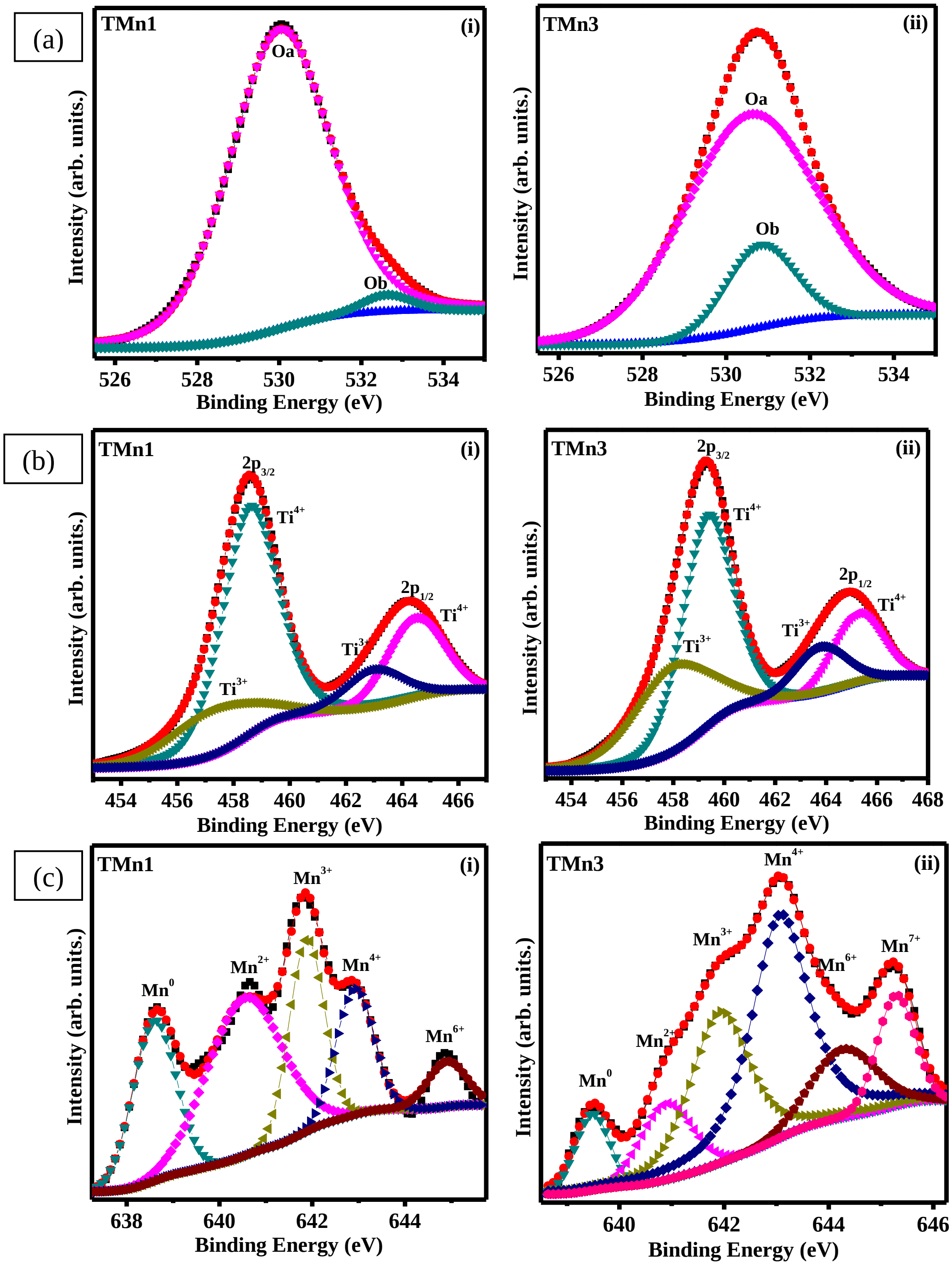

Figure 4.5 *XPS patterns of (a) O1s, (b) Ti 2p and (c) Mn 2p of* $Ti_{1-x}Mn_xO_2$ *(x=0.01 and 0.03).*

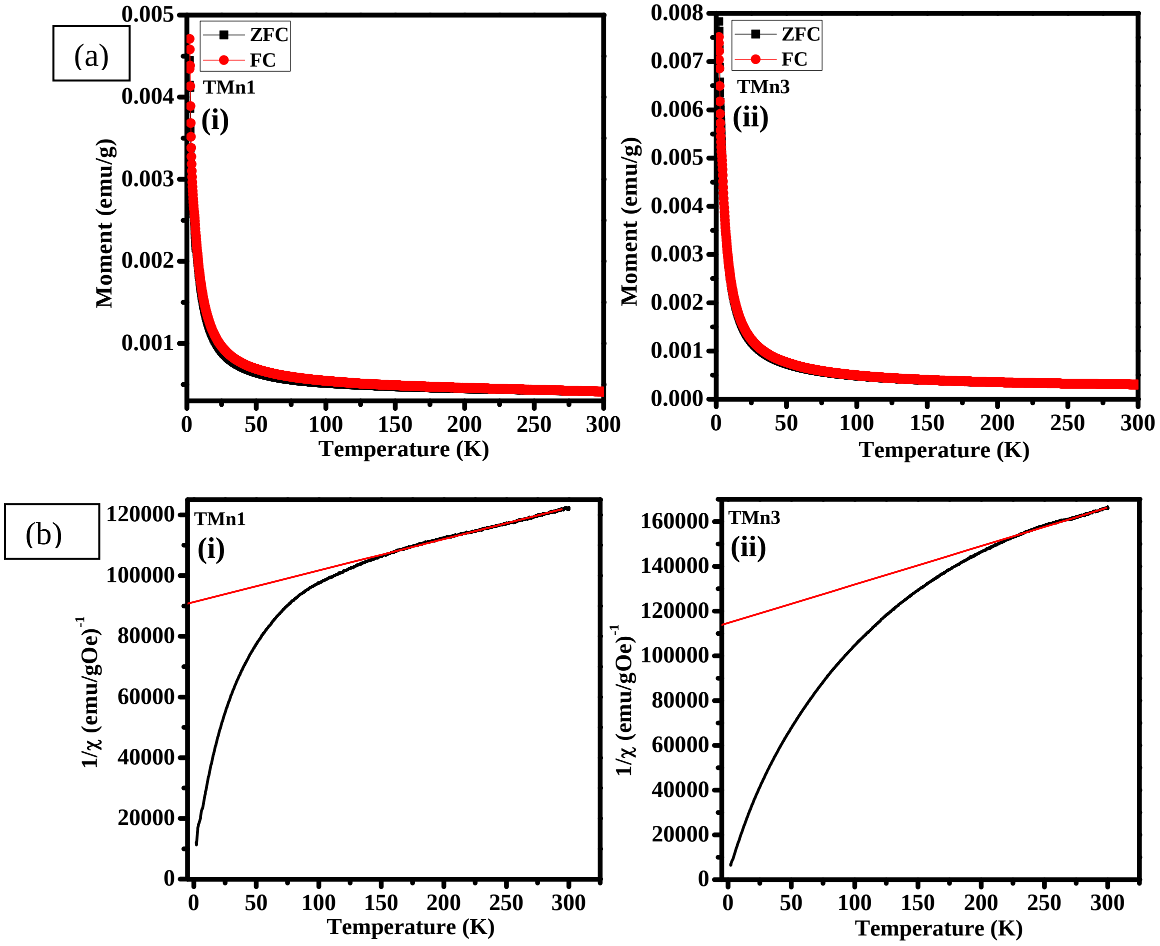

Figure 4.6 *(a) Temperature dependent magnetization under zero field cooling (ZFC) and field cooling (FC) at 50 Oe of* $Ti_{1-x}Mn_xO_2$ *(i)* $x = 0.01$ *and (ii)* $x = 0.03$*, (b) show corresponding temperature dependent inverse susceptibility.*

of TMn1 is fitted to five peaks corresponding to oxidation states, 0, 2+, 3+, 4+ and 6+. In TMn3, the Mn $2p_{3/2}$ peak is fitted with six peaks, assigned to 0, 2+, 3+, 4+, 6+ and 7+ oxidation states of Mn. Moreover, one may note that with increasing Mn doping, the concentration of lower valency Mn ions decreases at the expense of higher one, corroborates with the creation of Ti^{3+} ions. The presence of Ti^{3+} is the origin of magnetism in diamagnetic TiO_2. Therefore, further we have study the magnetic properties of both the samples, TM1 and TM3.

4.3 Magnetic Property

In this section, we have discussed the magnetic properties by carrying out temperature dependent magnetization (M-T) and field dependent magnetization (M-H).

4.3.1 Temperature Dependent Magnetization

Temperature dependent magnetization measured under zero field cooling (ZFC) and field cooling (FC) in the presence of 50 Oe field is shown in Figure 4.6 (a). Both curves match with each other from RT to 2 K except small kinks at 5 and 7 K. A sharp change is observed in magnetization of FC and ZFC curves at ~10 K. The steady increase in magnetization on lowering the temperature indicates the presence of frozen isolated Mn ions in the host TiO_2 lattice that contribute to paramagnetic ordering. Choudhury et al. (2013)b, reported that with increasing concentration of Mn, a prominent peak is found to be located at ~40 K which is an indication of Mn_3O_4. In contrast, we do not observe such peak down to 10 K which eliminates the presence of magnetic phase formed by Mn and O. In Figure 4.6 (b) inverse magnetic susceptibility curves are shown which intersects the temperature axis at -885 and -669 K for TMn1 and TMn3, respectively. The negative sign of the Curie–Weiss temperature, θ, indicates that the magnetic interactions are strongly antiferromagnetic in nature.

4.3.2 Field Dependent Magnetization

Magnetization versus field (M-H) plots at 10 K, show the presence of hysteresis loop in the range of applied magnetic field (± 70 kOe) indicating the signature of FM irrespective of phase and crystallinity at low temperature, shown in Figure 4.7. Such FM observed in Mn doped TiO_2 is ascribed to the interfacial defects such as oxygen vacancies [Zhang et al. (2016)]. Choudhury et al. (2013)b, however, explain the interaction of neighboring Mn^{2+}

ions through oxygen vacancies (F^+ centers) giving rise to the ferromagnetic behavior in Mn doped TiO_2. In our case, in addition to oxygen vacancies, the various oxidation states of Mn and Ti could serve the purpose of FM in these samples. Due to various oxidation states, one may expect prominent photocatalytic behavior in these samples like in TiO_2 nanoparticles discussed in last chapter.

4.4 Photocatalytic Property

In order to examine the photocatalytic degradation of organic dyes like MB, RhB and CR using these samples, we have determined the band gap using UV-Visible spectrophotometer. The band gap of TMn1 and TMn3 are found to be 3.1 and 3.3 eV, respectively. The band gap around 3 eV is favorable for photocatalysis under visible light.

Here, we have carried out photocatalysis using TMn1 and TMn3 under renewable source of energy, sunlight. Time dependent absorption spectra of the degraded dye solutions have been recorded as shown in Figure 4.8 (a) and (b), for TMn1 and TMn3, respectively. The absorption spectra show λ_{max} at 665, 550 and 500 nm, for MB, RhB and CR, respectively. The rate of dye degradation is recorded with respect to change in intensity of absorption peak. The highest intense peak in these spectra corresponds to highest concentration of the dye solution. The decrease in intensity of the peak with time indicates reduction in concentration of the dye in solution, due to degradation of the dye. In this case, Mn doped TiO_2 generates electron–hole pair under sunlight. The electron reduces oxygen and hole oxidizes water which produces the highly reactive species like superoxide and hydroxyl radicals, respectively. These highly reactive species react with organic impurity leading to degradation of dyes [Bagwasi et al. (2013)]. The degradation percentage of the dyes calculated using equation: Degradation % = $[(C_0\text{-}C)/C_0] \times 100)$ (where C_0 is the initial

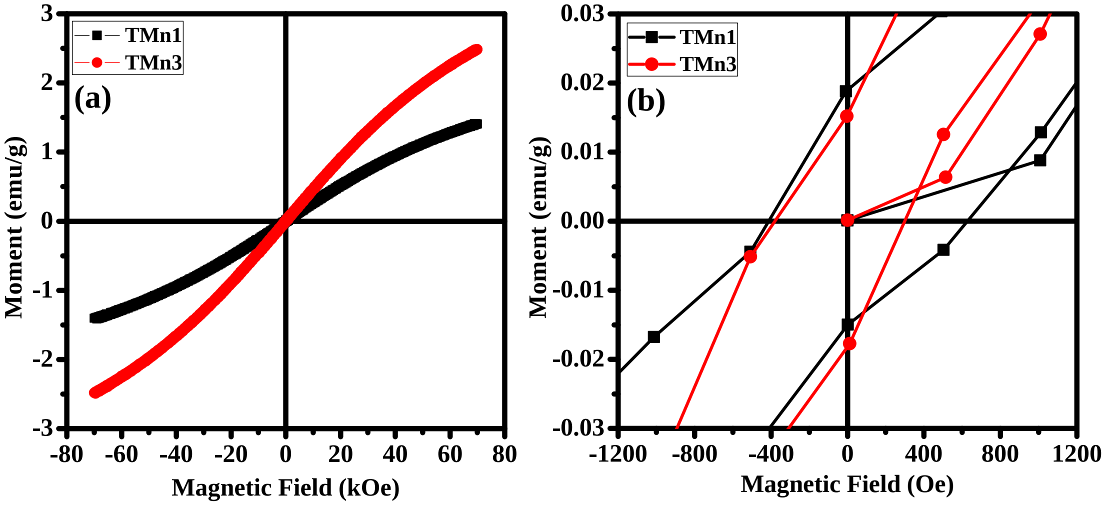

Figure 4.7 *(a) M vs H of* $Ti_{1-x}Mn_xO_2$ *(x =0.01 and 0.03) at 10 K, (b) zoomed view of M-H plot.*

(a)

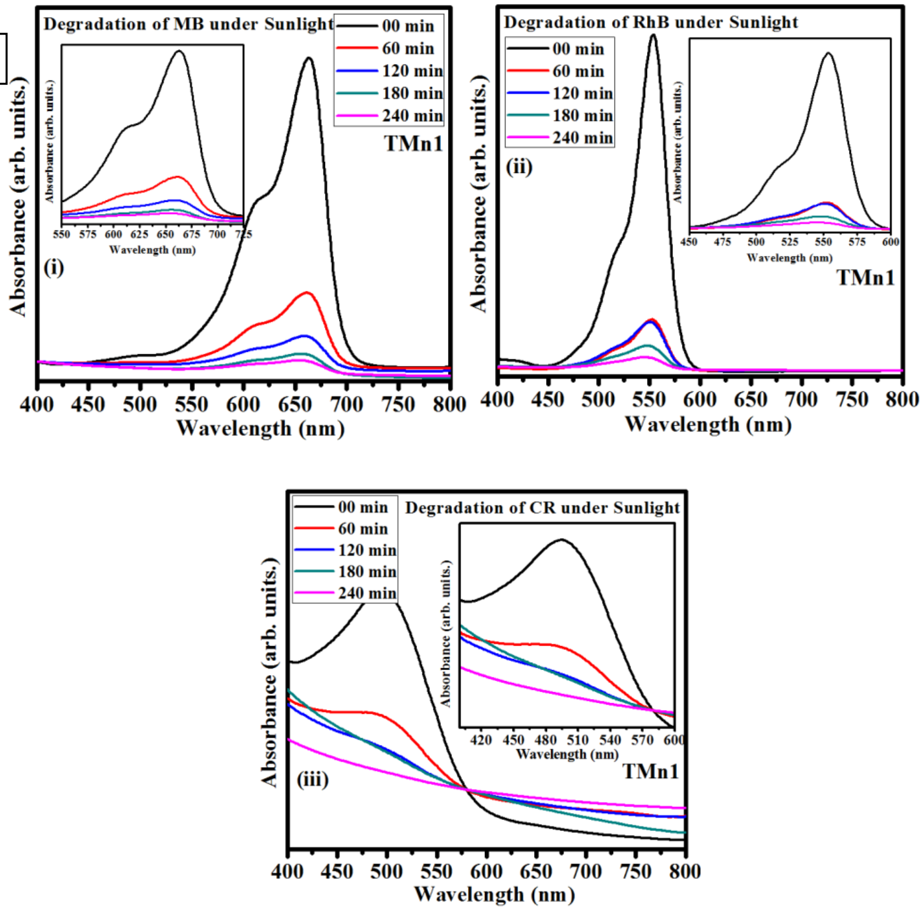

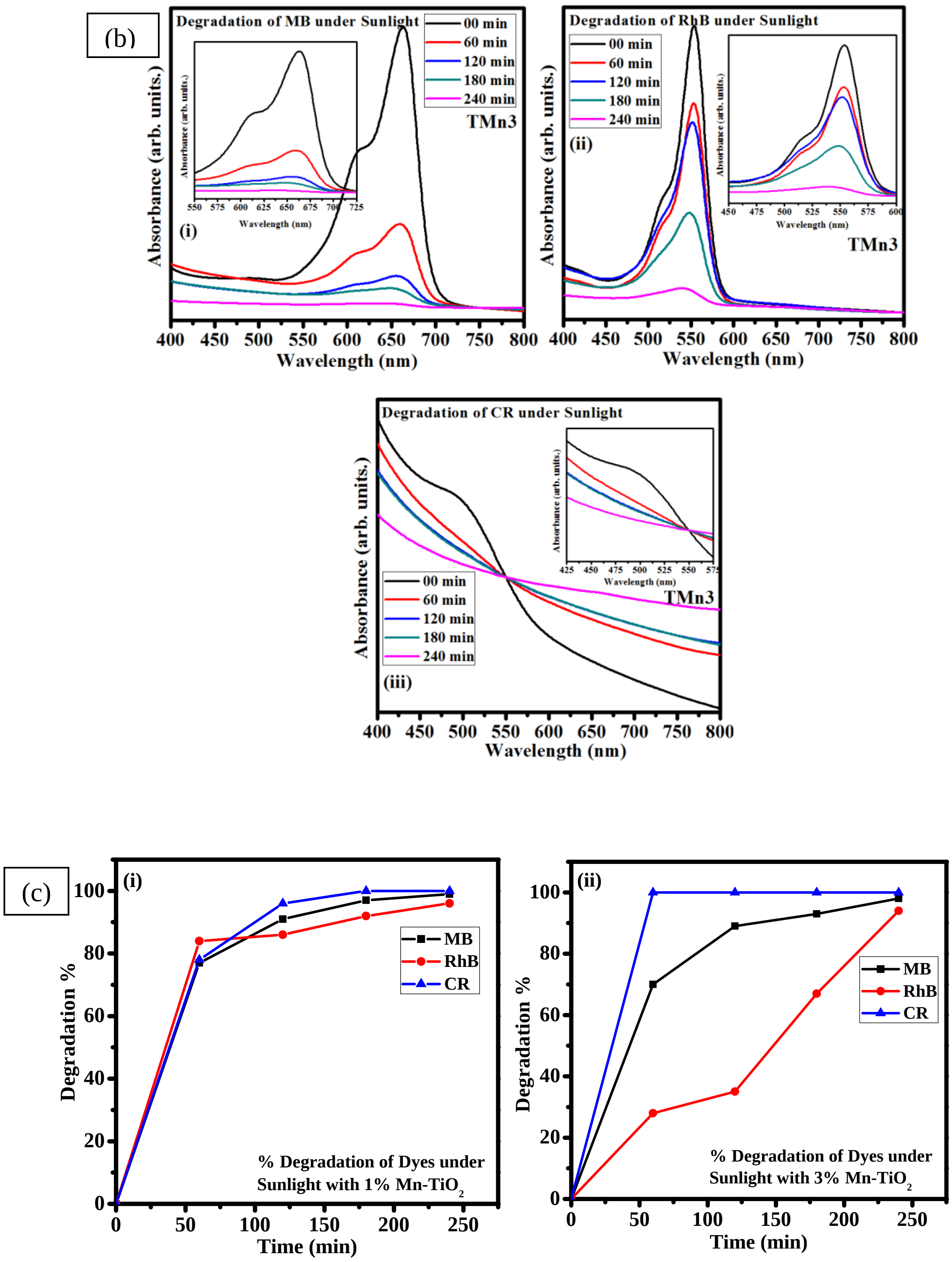

Figure 4.8 *UV-visible absorption spectra of MB, RhB and CR solution before and after irradiation with sunlight using* $Ti_{1-x}Mn_xO_2$ *(a)* $x = 0.01$ *and (b)* $x = 0.03$*; (c) Degradation rate of MB, RhB and CR (i)* $x = 0.01$ *and (ii)* $x = 0.03$.

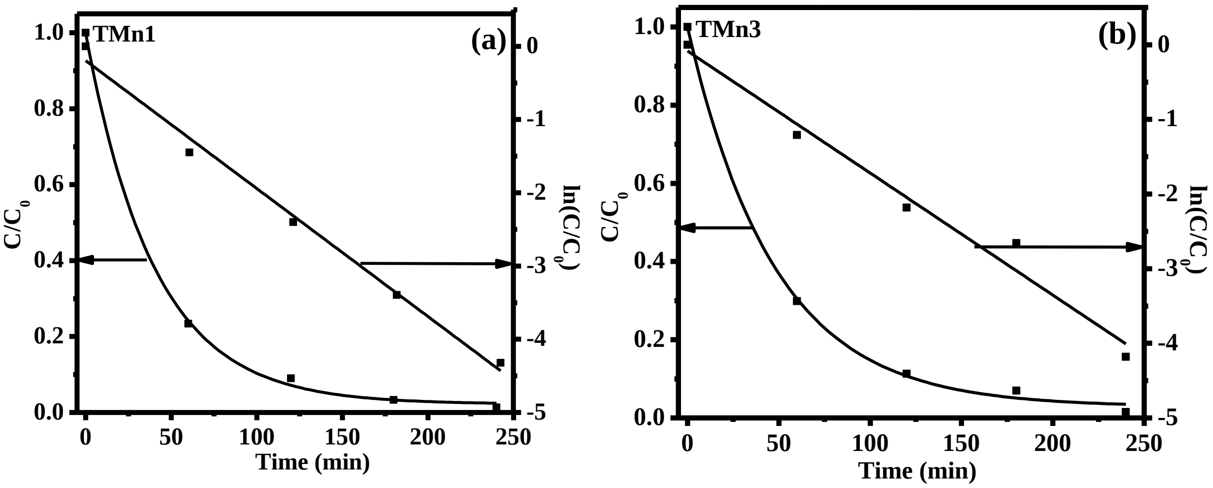

***Figure 4.9** Degradation profile of MB using $Ti_{1-x}Mn_xO_2$ (a) x = 0.01 and (b) x = 0.03, under sunlight.*

concentration and C is the concentration of dye solution after time t) is shown in Figure 4.8 (c). TMn1 show about 80% degradation of all three dyes after 1 h, and TMn3 degrades 100% CR and about 80% MB in 1 h. While 100% of CR degrades after 3 h of irradiation, 99 and 96% of MB and RhB, degrade after 4 h using TMn1. After 4 h of irradiation, 94 to 98% of MB and RhB degrade using TMn3. The degradation profiles show exponential decay with time which confirms the first-order kinetics (Figure 4.9). Previous literatures report degradation of various dyes using Mn, Bi, B doped TiO_2 using visible light, UV and simulated light [Chauhan et al. (2012), Binas et al. (2012), Bagwasi et al. (2013) and Deng et al. (2011)]. However, the rate of degradation is less. In this case, for the first time, we demonstrate 100% photocatalytic degradation of dyes under sunlight using only 20 mg of Mn doped TiO_2 samples, which could possible not only due to the band gap but also the phase, surface area, size and oxygen vacancies accompanied with different oxidation states of Mn and Ti. The presence of oxygen vacancies result in formation of Ti^{3+} on the surface of TiO_2, can trap photogenerated electrons and leave behind unpaired charges to promote photocatalytic activity. Growth inhibition or killing of bacteria using TiO_2 is widely investigated [Fu et al. (2005), Wanag et al. (2018)]. Therefore, in addition to degradation of dyes here we examine the antibacterial property of the Mn doped TiO_2 samples.

4.5 Antibacterial Property

Antibacterial property of TiO_2 and Mn doped TiO_2 are investigated using MTT (3(4, 5- dimethylthiazol-2-Yl)-2, 5-diphenyl tetrazolium bromide) assay. The S.Aureus (MTCC# 435) bacteria are used for this antibacterial study. All samples at concentration 10 mg/mL are incubated with S.Aureus suspension for 24 h. The inhibition rate of the bacteria S.Aureus after treating with the sample TM1 and TM3 at a very low concentration (10 mg/mL) of sample is shown in Figure 4.10. It is observed that the rate of inhibition is more in both the samples compared to the control. This indicates that both the samples show antibacterial effect towards S.Aureus. The bactericidal effect of TiO_2 generally has been attributed to the decomposition of bacterial outer membranes by reactive oxygen species (ROS), primarily hydroxyl radicals (·OH), which leads to phospholipid peroxidation and ultimately cell death [Xing et al. (2012) and Fu et al. (2005)] . Fu et al. (2005) studied antibacterial property of gold coated TiO_2 and vanadium doped TiO_2 nanoparticles against the bacteria E. coli (DH 5R) and Bacillus megaterium (QM B1551). However, Wanag et al. (2018) report, that reduced graphene oxide and TiO_2 composite exhibits higher antibacterial activity than that of pure TiO_2 synthesised through hydrothermal technique. In another report, enhanced antimicrobial activity is found in the TiO_2 NPs modified with G. zeylanica [Senarathna et al. (2017)]. Xing et al. (2012), examined the antibacterial property of polyethene films after incorporating with TiO_2 nanoparticles against the bacteria S. aure-

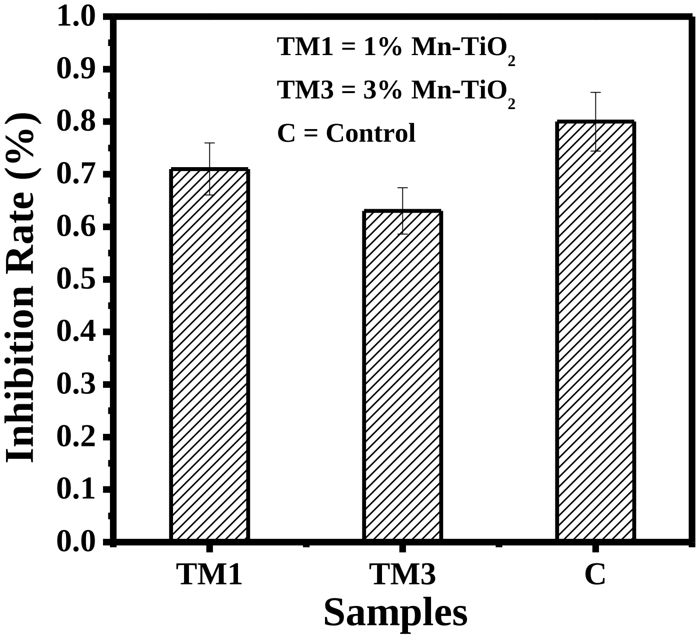

Figure 4.10 *Antibacterial activity of Mn doped TiO_2 against S.Aureus.*

us. Antibacterial activity against bacteria, E.Coli is studied with TiO_2 nanoparticles synthesised by laser abalation and found that sample has antibacterial nature [Zimbone et al. (2015)]. Here, we observed antibacterial effect in Mn doped TiO_2, which is not reported earlier.

4.6 Conclusions

In this chapter, Mn doped TiO_2 nanoparticles with 1, 2 and 3 at% of Mn were synthesized by a simple, cost effective and viable sol-gel technique followed by calcination at 500 ºC. While XRD patterns showed the mixed phase of anatase and rutile for 1 and 2 at% of Mn doped TiO_2, 3 at% Mn doped TiO_2 exhibited pure anatase phase. Such phase transformation from mixed anatase and rutile phase to anatase one with increasing Mn concentration was not reported earlier. The particles of 15 and 12 nm estimated from TEM were of single crystalline nature observed from SAED patterns. From XPS, it was observed that oxygen vacancies present in all the samples were accompanied with various oxidation states of Ti and Mn. As a result, we observed a ferromagnetic behavior. In addition, we successfully demonstrated 100% photocatalytic degradation of CR and more than 80% degradation of MB in 1 h using only 20 mg of Mn doped TiO_2 under sunlight irradiation. Such promising performance of Mn doped TiO_2 for dye degradation hold great potential to purify the industrial waste water. Besides photocatalytic property both the sample showed the antibacterial property against the S.Aureus bacteria.